Nanocomposites from Solution-Synthesized PbTe-BiSbTe Nanoheterostructure with Unity Figure of Merit at Low-Medium Temperatures (500–600 K)

Biao Xu, Matthias T. Agne, Tianli Feng, Thomas C. Chasapis, Xiulin Ruan, Yilong Zhou, Haimei Zheng, Je-Hyeong Bahk,* Mercouri G. Kanatzidis, Gerald Jeffrey Snyder,* and Yue Wu*

More than 50% of the world's energy consumption is wasted in the form of heat, and thermoelectric energy conversion is attracting great attention as an effective and reliable method to recover this waste heat as electricity.[1] The efficiency of a thermoelectric material is determined by its dimensionless figure of merit, $zT = S^2\sigma T/(\kappa_e + \kappa_l + \kappa_{bi})$, where S is the Seebeck coefficient, σ is the electrical conductivity, T is the operating temperature, and κ_e, κ_l, and κ_{bi} are the electronic, lattice, and bipolar contributions to thermal conductivity, respectively. Maximizing zT requires the simultaneous enhancement of the power factor ($S^2\sigma$) and reduction of the thermal conductivity (κ_{tot}). Band engineering with resonant levels,[2] band convergence,[3] energy filtering effects,[4] and quantum confinement[5] are widely explored to enhance $S^2\sigma$. To reduce κ_{tot}, materials with an intrinsically low κ_l are used as the starting material.[6] Nanostructuring[7–9] and defect engineering[10] lead to further reduction in κ_l. As κ_{bi} is determined by electronic transport,

Dr. B. Xu, Prof. Y. Wu
Department of Chemical and Biological Engineering
Iowa State University
Ames, IA 50011, USA
E-mail: yuewu@iastate.edu
M. T. Agne, Dr. T. C. Chasapis, Prof. G. J. Snyder
Department of Materials Science and Engineering
Northwestern University
Evanston, IL 60208, USA
E-mail: jeff.snyder@northwestern.edu
T. Feng, Prof. X. Ruan
School of Mechanical Engineering
Purdue University
West Lafayette, IN 47907, USA
Dr. Y. Zhou, Prof. H. Zheng
Materials Sciences Division
Lawrence Berkeley National Laboratory
Building 62 Room 211, 1 Cyclotron Road, Berkeley, CA 94720, USA
Prof. J.-H. Bahk
Department of Mechanical and Materials Engineering
University of Cincinnati
Cincinnati, OH 45221, USA
E-mail: bahkjg@uc.edu
Prof. M. G. Kanatzidis
Department of Chemistry
Northwestern University
Evanston, IL 60208, USA

it can be mitigated by degenerately doping the semiconductor and/or alloying it with larger-bandgap compounds.

Since the 1950, Bi_2Te_3-based alloys ($Bi_xSb_{2-x}Te_3$ and $Bi_2Te_{3-x}Se_x$) have been widely used and commercialized for refrigeration and thermoelectric energy conversion applications in the low-temperature range (300–450 K).[11–13] However, at higher temperatures (>500 K), their zT value decreases substantially, mainly due to the onset of bipolar conduction that arises from low carrier concentrations and its small bandgap ($E_g \approx 0.18$ eV). At mid-range temperatures (600–900 K), good candidates are mainly limited to PbTe alloys ($E_g \approx 0.31$ eV).[14] Thus, combining p-type BiSbTe and PbTe may yield good thermoelectric materials with a peak zT value located in the low-medium temperature range (500–600 K). Indeed, aliovalent Pb, with less valence electrons than Bi(Sb), can act as an extrinsic acceptor for p-type BiSbTe.[15] Similarly, doping with other elements (Ag,[16] In,[17] Cu,[18] Zn[19]) may allow further tuning of the carrier concentration, thus optimizing the power factor and shifting the peak zT toward higher temperatures, but at the cost of carrier mobility. Carrier concentration can also be modified through defect engineering (e.g., Sb/Te antisites), although limitedly.[12,20] On the other hand, nanostructuring can suppress lattice thermal conductivity (κ_l).[8] Nanosizing was also proposed to suppress κ_{bi} through selectively blocking minority carriers in BiSbTe, although limited to below 400 K.[8,21] Additionally, alloying/doping may tailor the bandgap and Fermi level, diminishing bipolar conduction. Alas, without synergistic optimization of these interdependent parameters, unity zT cannot be achieved in Bi_2Te_3-based materials from 500 to 600 K, where the application of thermoelectrics is promising for the recovery of low-grade waste heat. Furthermore, conventional solid-state synthesis[22] requires high-temperature, energy-consuming processes to alloy or dope, with poor control over grain size. In contrast, solution synthesis has provided a more sustainable and efficient route to both doping/alloying and nanostructuring,[23] inspiring us to improve the performance of Bi_2Te_3.

Herein, we report the thermoelectric properties of Pb-doped BiSbTe nanocomposites derived from a scalable, solution-synthesized precursor made in 10 g batches. The nominal compositions are $Bi_{0.7}Sb_{1.3}Te_3$ with 0–4.0 at% Pb dopants. The as-obtained nanocomposites show an optimized power factor ($S^2\sigma$) that peaks at a higher temperature than previous BiSbTe compounds, a strongly reduced κ_l as compared to bulk-grain counterpart, a remarkably suppressed κ_{bi}, and a high zT (≈ 1.0)

COMMUNICATION

in the range of 513–613 K. This pushes the working temperature of conventional BiSbTe materials ≈100 K higher.

The low-temperature solution-phase synthesis is based on a three-step strategy developed by our group.[24,25] In Step 1, tellurium dioxide, potassium hydroxide, and polyvinylpyrrolidone (M_w = 40 000) are dissolved into ethylene glycol (EG). The pale yellow solution is then heated to 100 °C and hydrazine hydrate (80%) is injected. The solution turns into a dark blue slurry, indicative of the formation of tellurium (0). It is kept at 100 °C for 1 h before the temperature is raised to 110 °C. In Step 2, a solution of lead acetate trihydrate is added drop wise into the dispersion of Te nanowires at 110 °C. Then another 1 h of heating is maintained for the formation of the PbTe-Te-PbTe nanoheterostructure. In Step 3, an EG solution of Bi and Sb precursors (bismuth nitrate pentahydrate and antimony acetate) is added drop by drop, with precedent injection of anhydrous hydrazine. The black slurry is heated at 110 °C for 1 h and then incubated at 140 °C for another 8 h before the production of the PbTe-BiSbTe-PbTe nanoheterostructure.

Comprehensive characterization is performed to examine the structure and composition of the intermediate product at each step of the synthesis. First, X-ray diffraction (XRD) patterns are recorded to verify the crystal phases. After Step 1, pure Te (trigonal, JCPDS-#36-1452) is indexed and no impurity such as TeO_2 is found (**Figure 1**a). This corroborates the reducing ability of hydrazine hydrate, as evidenced by its wide use in efficient synthesis of Te nanostructures.[25] After Step 2, the diffraction peaks of both Te and PbTe (face centered cubic, JCPDS-#38-1435) are discerned, indicating that PbTe has been incorporated (Figure 1a). After Step 3, the XRD profile shows peaks of PbTe, Te, and $Bi_xSb_{2-x}Te_3$ (hexagonal, x = 0.5
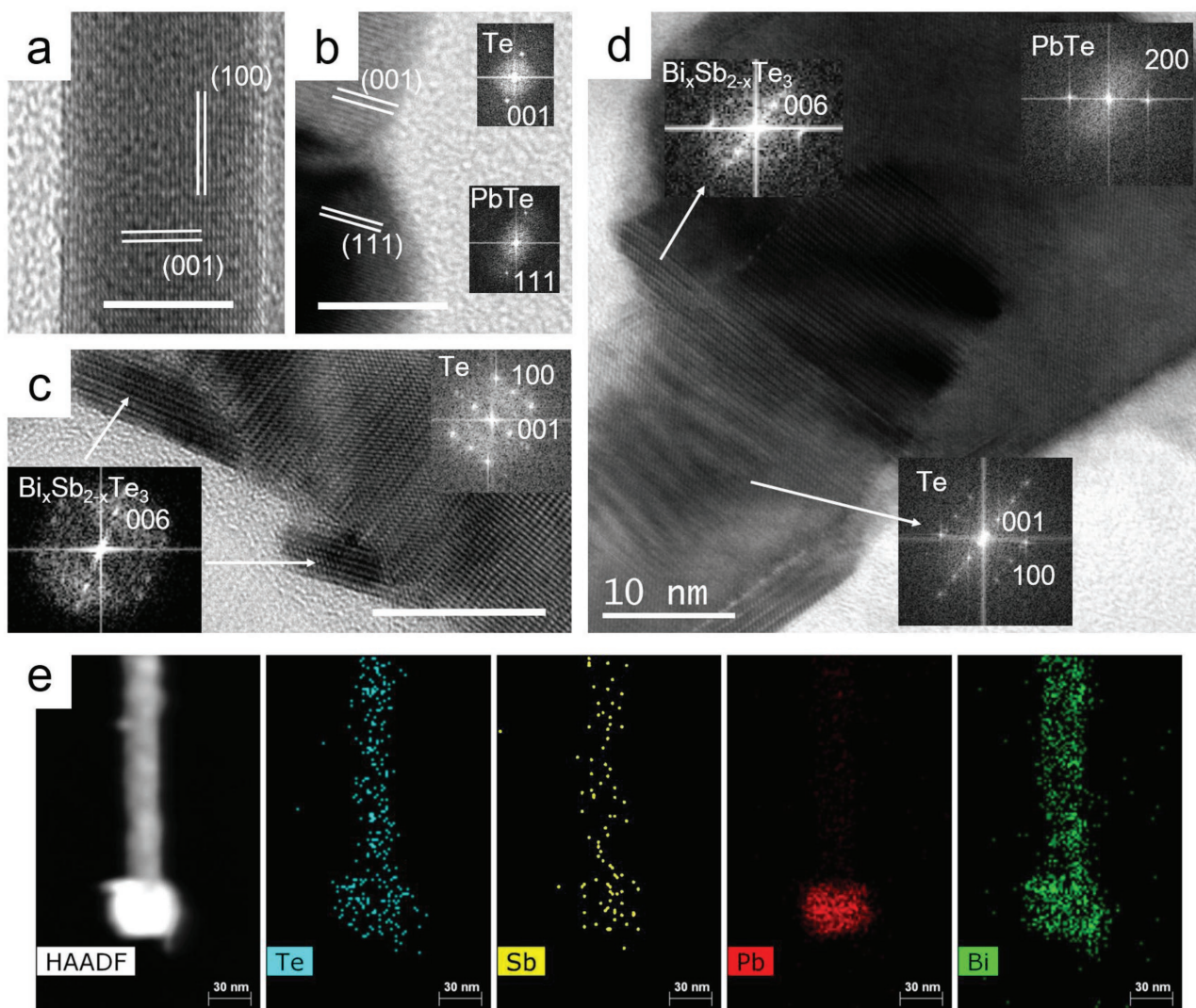
for JCPDS-#49-1713) (Figure 1a). However, as some reflection peaks of Te, PbTe, and $Bi_xSb_{2-x}Te_3$ overlap with each other, transmission electron microscopy (TEM) investigation is needed for further clarification.

The compositions of the aforementioned nanostructures are further verified by our TEM study. First, the 1D shape of the Te nanowire, produced in Step 1, is clearly observed (Figure 1b). Statistics of the nanowire diameter reveal a narrow distribution (17 ± 2 nm) and the length of nanowires is found to be 1500 ± 200 nm. The (001) lattice fringe of Te (**Figure 2**a) that is perpendicular to the axial direction indicates that the nanowire grows along the c axis. Second, in Figure 1c, the barbell-like morphology of the PbTe-Te-PbTe nanoheterostructure is displayed. The (111) plane of PbTe can be seen on the tips and is parallel with the (001) plane of Te wire part (Figure 2b). After step 3, all the crystal domains of Te, PbTe, and $Bi_xSb_{2-x}Te_3$ can be found in the as-obtained PbTe-BiSbTe-PbTe nanoheterostructure (Figure 1d and 2c,d). The PbTe (002) lattice fringe is found on the tip. A fast Fourier transform (FFT) pattern along the Te [010] zone axis is observed on the nanowire body. The typical layered structure and (006) spot of $Bi_xSb_{2-x}Te_3$ in FFT are seen on the sidewall of the nanowire (Figure 2c) and also the junction of the wire and the tip (Figure 2d). This indicates that $Bi_xSb_{2-x}Te_3$ is grown from the reaction of Bi and Sb atoms with surface Te atoms. High angular annular dark field-scanning transmission electron microscopy (HAADF-STEM) and elemental mapping also corroborate that PbTe is grown on the tip, while the nanowire body is comprised of $Bi_xSb_{2-x}Te_3$ and unreacted Te (Figure 2e).

Scanning electron microscopy (SEM) images further verify the morphology of products step-by-step (Figure S1–S4,
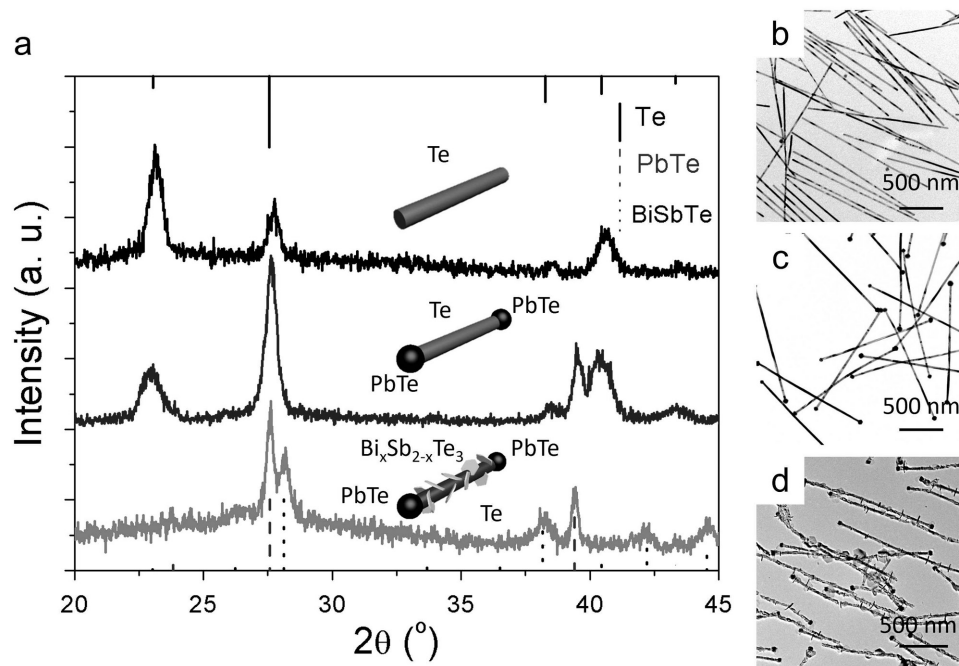
Figure 1. Characterization of the intermediate products of the PbTe-BiSbTe nanoheterostructure. a) XRD patterns of Te (top) after step 1, 0.04 PbTe-Te-PbTe (middle) after step 2, and 0.04 PbTe-BiSbTe-PbTe (bottom) after step 3; the solid lines are indicative of tellurium, the dashed ones are PbTe, and dotted ones represent $Bi_{0.5}Sb_{1.5}Te_3$. Transmission electron microscopy images of b) Te nanowire, c) 0.04 PbTe-Te, and d) 0.04 PbTe-BiSbTe nanoheterostructure.

ADVANCED
SCIENCE NEWS
www.advancedsciencenews.com

ADVANCED
MATERIALS
www.advmat.de

COMMUNICATION

Figure 2. HRTEM study on intermediate products of the PbTe-BiSbTe nanoheterostructure. HRTEM images of a) the Te nanowire after step 1, b) the 0.04 PbTe-Te-PbTe nanoheterostructure after step 2, c) the wire part and d) the junction area of the 0.04 PbTe-BiSbTe-PbTe nanoheterostructure after step 3. The insets show corresponding fast Fourier transform (FFT) patterns. All scale bars in (a)–(d) represent 10 nm. e) HADDF-STEM image and EDS elemental mapping of the 0.04 PbTe-BiSbTe-PbTe nanoheterostructure; the scale bar is 30 nm.

Supporting Information). Energy-dispersive spectrum (EDS) also provides strong evidence that the Te nanowire is only partially converted to BiSbTe in the PbTe-BiSbTe-PbTe nanoheterostructure. Taking the "0.015 Pb" sample as an example, the atomic ratio of Pb:Bi:Sb:Te is 1.5:16.3:49.0:100 in the precursors. While the atomic ratio in the final product is Pb:Bi:Sb:Te = 1.4:16.9:27.9:100. It is clear that Pb, Bi, and Te are mostly converted, whereas only ≈57% (27.9/49.0) of Sb is reacted.

The successful synthesis of the PbTe-BiSbTe nanoheterostructure and its structural integrity may originate from the delicate match in atomic structure of each constituent phase. According to high resolution transmission electron microscopy (HRTEM) analyses (Figure 2), we construct atomic structure models for PbTe (111)-Te (001), $Bi_xSb_{2-x}Te_3$ (001)-Te (001), and PbTe (111)-$Bi_xSb_{2-x}Te_3$ (001) interfaces (Figure S5–S10, Supporting Information). In these models, the dangling bonds are well saturated and the coordination geometry is finely retained

at the interfaces. The nice match in crystal structures also brings about the generality in synthesis. The composition of these PbTe-BiSbTe-PbTe nanoheterostructures is tunable over a wide range (0.5–4.0 at% Pb, see the Experimental Section in the Supporting Information; Figure S3 and S4 of the Supporting Information and Figure 2). This provides us with a rich library of potentially new materials. The other important feature of our synthesis is the 10 g scale (**Figure 3**a, inset). To the best of our knowledge, this is the first synthesis of nanoheterostructures in such an energy-saving, repeatable and scalable way. The scalable synthesis of nanoheterostructures will pave the way for applications not only in thermoelectrics but also in other fields, such as photocatalysis, electronics, and optoelectronics.[26]

The tunable, repeatable, and scalable synthesis of PbTe-BiSbTe nanoheterostructures allows us to fabricate bulk nanocomposites. The nanoheterostructures are washed by an ethanol solution of hydrazine and then vacuum dried.[24] The
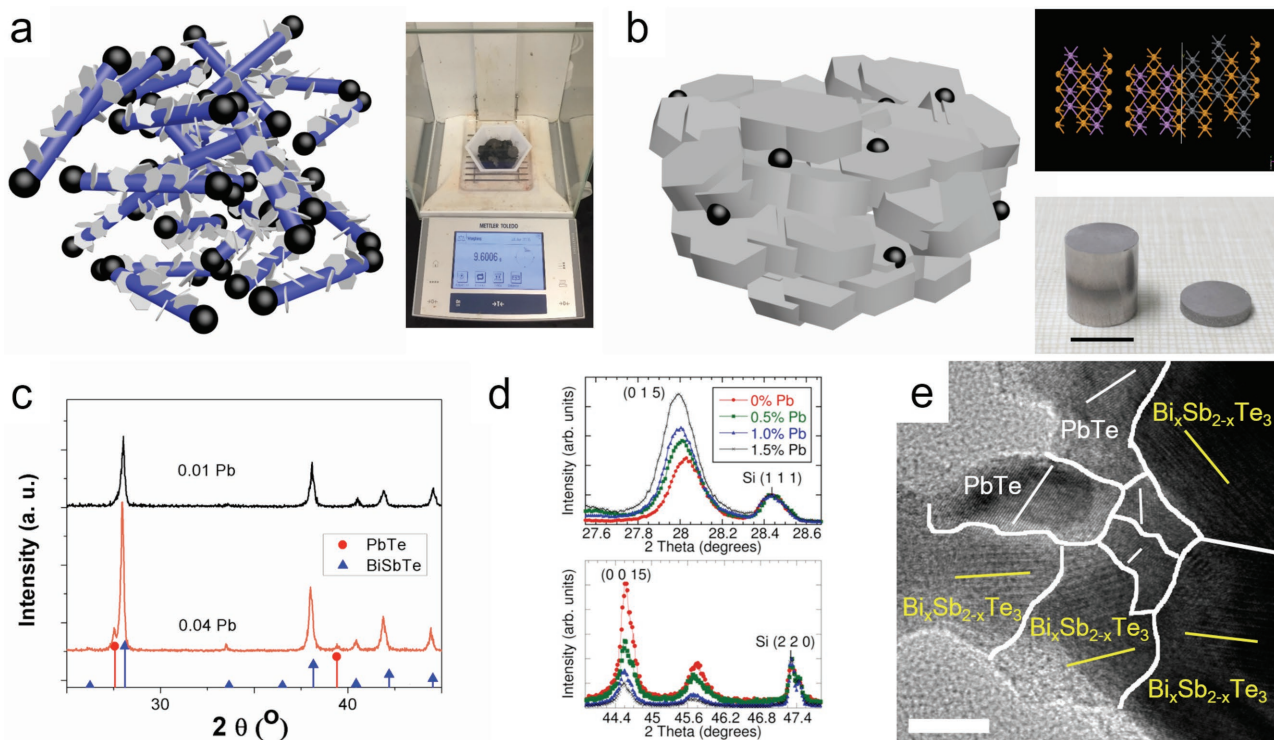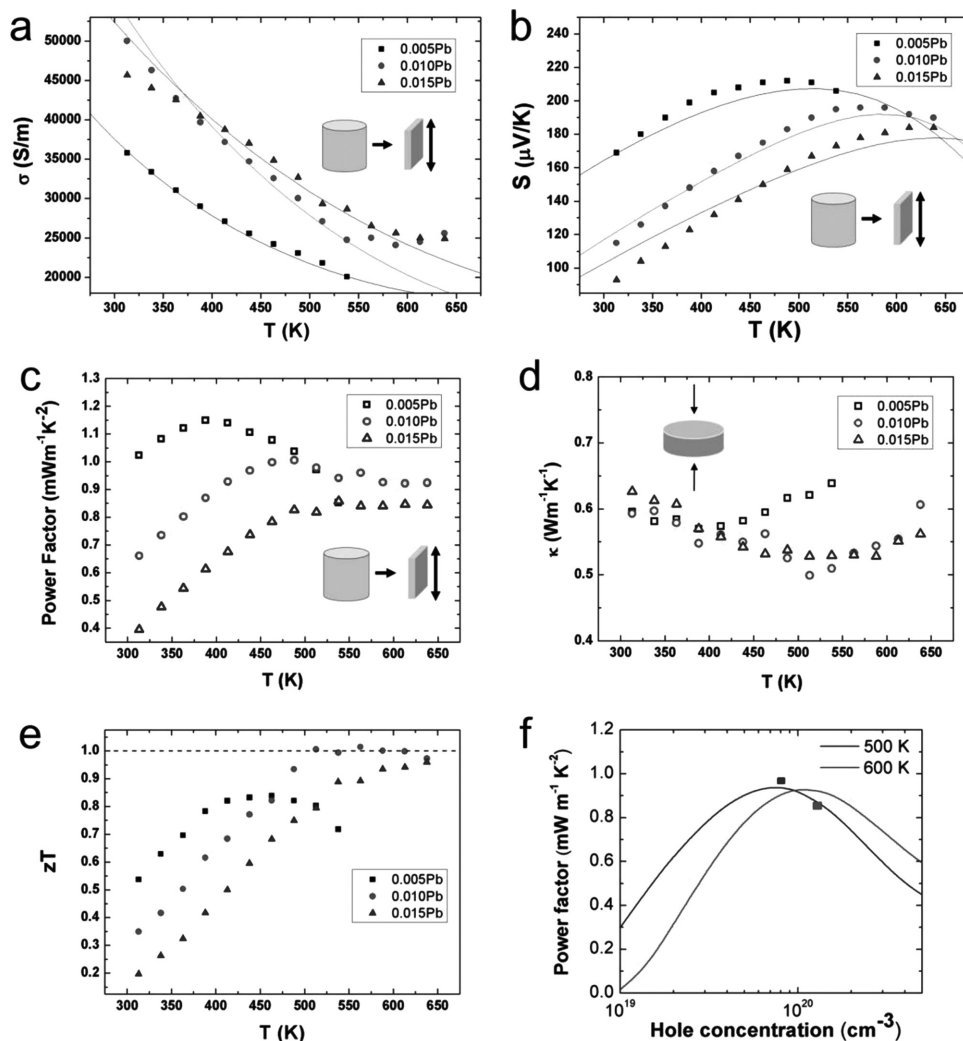
Figure 3. Characterization of the Pb-BiSbTe nanocomposites after SPS. a) Schematic illustration and digital image of 9.6 g of nanoheterostructures before SPS; b) Schematic illustration of as-pressed Pb-BiSbTe nanocomposite, atomic structure of PbTe-BiSbTe interface (purple: Bi/Sb; gray: Pb; and orange: Te) and digital image of the SPSed cylinder and disk; scale bar is 10 mm. c) XRD profiles of the 0.01 PbTe and 0.04 PbTe-$Bi_{0.7}Sb_{1.3}Te_3$ bulk nanocomposites. The red drop line indicates PbTe and the blue one corresponds to $Bi_{0.5}Sb_{1.5}Te_3$; d) XRD peak shifts corresponding to increased lattice parameters with nominal Pb doping; e) HRTEM image of 0.04 PbTe-$Bi_{0.7}Sb_{1.3}Te_3$ bulk nanocomposite. The white lines depict lattice fringes of PbTe and the yellow ones stand for those of BiSbTe. The scale bar is 10 nm.

dried chunk is ground into a fine powder and filled into a phi-10.0 mm (inner diameter) graphite die in a glove box. Then the tooling is loaded in a Fuji-211lx Spark Plasma Sintering (SPS) system where it is put under vacuum and subjected to a uniaxial pressure of 40 MPa, heated and kept at 425 °C for 5 min. The as-obtained disk is polished and shows metallic luster (Figure 3b, inset).

The compositions of the SPSed disks are checked via EDS. For the 0.015 Pb sample, the Pb:Bi:Sb:Te molar ratio is around 1.4:16.1:30.2:71.1. Compared with the nanoheterostructure before SPS (Pb:Bi:Sb:Te molar ratio = 1.4:16.9:27.9:100), it is clear that the ratio among Pb, Bi, and Sb is almost unchanged. In contrast, there is a 28.9% loss of Te. Before SPS, the molar ratio of Te/(Bi+Sb) is 2.23 in the pristine powder, which is significantly larger than 1.50, a typical value for $Bi_{0.7}Sb_{1.3}Te_3$. The pristine powder can be regarded as Pb-$Bi_{0.7}Sb_{1.3}Te_3$ alloy plus excess elemental Te. According to the Te-rich region of the $Bi_xSb_{2-x}Te_3$-Te phase diagram,[10] the Te nanowire melts above ≈420 °C. Therefore, during the SPS process (≈425 °C), liquid Te is expelled out of the nanocomposite, leaving $Bi_{0.7}Sb_{1.3}Te_3$ nanoflakes and PbTe nanograins compressed together (Figure 3b), with an effective grain size of 40–60 nm (Figure 3e). In the final nanocomposite, the molar ratio of Te/(Bi+Sb) is 1.53, which is quite approximate to the stoichiometric value of 1.50. Similar trends are also found in the 0.01 Pb sample. Before SPS, the Pb:Bi:Sb:Te molar ratio is

around 0.8:17.1:25.7:100. After SPS it is 0.8:16.1:28.1:70.0. The Pb:Bi:Sb:Te molar ratio in the after-SPS 0.005 Pb sample is 0.4:14.0:25.2:60.2. For the undoped (0% Pb), after-SPS, sample the Bi:Sb:Te molar ratio = 14.3:25.6:60.2.

In the final PbTe-$Bi_{0.7}Sb_{1.3}Te_3$ nanocomposites, Pb may be dissolved in $Bi_{0.7}Sb_{1.3}Te_3$ or precipitate out as PbTe inclusion.[27] In SEM-EDS elemental mapping of 0.01 PbTe-$Bi_{0.7}Sb_{1.3}Te_3$, Pb is found to be scattered throughout the sample (Figure S13, Supporting Information). The dissolution of Pb in $Bi_{0.7}Sb_{1.3}Te_3$ is revealed by the progressive shift in the XRD peak of $Bi_{0.7}Sb_{1.3}Te_3$ (0 1 5) and (0 0 15) toward lower 2θ (higher interplane distance; Figure 3d), as the atomic radius of Pb is larger than Bi(Sb). The dissolved Pb is expected to act as an acceptor to parent $Bi_{0.7}Sb_{1.3}Te_3$ because there is one less valence electron in Pb ($6s^26p^2$) than in Bi ($6s^26p^3$, Sb, $5s^25p^3$). This leads to p-type conduction in the as-obtained disk, as is proved by the Hall effect measurement (Figure S14a, Supporting Information). The efficient doping of Pb may be aided by the small grain size of the starting PbTe-BiSbTe nanoheterostructures, which readily facilitates diffusion of Pb into BiSbTe during SPS. For the 0.01 Pb sample, the reflection peaks of PbTe are not detectable in XRD (Figure 3c). As the concentration of Pb increases (e.g., for 0.04 Pb sample) and exceeds the solubility limit in BiSbTe, PbTe can precipitate out as inclusions, as proved by XRD (Figure 3c, lower pattern) and TEM (Figure 3e).

ADVANCED
SCIENCE NEWS
www.advancedsciencenews.com

ADVANCED
MATERIALS
www.advmat.de

COMMUNICATION

Figure 4. Measurements and simulations of thermoelectric properties. Temperature dependence of a) electrical conductivity, b) Seebeck coefficient, c) power factor, d) thermal conductivity, and e) figure of merit. f) BTE-calculated power factor ($S^2\sigma$) as a function of hole concentration (curves) with experimental values (markers). The markers in (a)–(f) are experimental values and the curves in (a), (b), and (f) are simulations.

The successful fabrication of PbTe-BiSbTe bulk nanocomposites with tunable composition enables us to investigate their thermoelectric properties. Unless intentionally noted, all measurements are conducted in the cross-plane direction (**Figure 4**; also see in-plane results in Figure S15, Supporting Information). Electrical conductivities (σ) of the 0.005, 0.010, and 0.015 Pb samples all decrease with ascending temperature, as is typical of heavily doped degenerate semiconductors (Figure 4a). While in the high-temperature intrinsic region, σ of the 0.010 Pb sample shows saturation. The 0.015 Pb sample has similar electrical conductivity with that of the 0.010 Pb sample and higher σ than that of the 0.005 Pb sample. Hole concentration (n_p) increases monotonically with increased Pb composition (8.00×10^{19} cm^{-3} for 0.010 Pb sample and 1.25×10^{20} cm^{-3} for 0.015 Pb sample; Figure S14a, Supporting Information) while the hole mobility (μ_p) shows the opposite trend (Figure S14b, Supporting Information).

Composition-dependent Seebeck coefficients (S) are presented in Figure 4b. For the 0.005, 0.010, and 0.015 Pb samples, the S have positive signs, agreeing well with the Hall-effect measurements showing a p-type transport behavior (Figure S14a, Supporting Information). The Seebeck coefficients increase steadily with rising temperature in the low-temperature range and then decrease afterward with elevated temperature. This roll-over behavior can be attributed to the thermal excitation of minority carriers (electrons) and their adverse contribution to the net Seebeck coefficient. The decreased Seebeck coefficients with respect to increased carrier concentration can be explained by the Pisarenko plot (S-n_H) (Figure S14g, Supporting Information). Power factors ($S^2\sigma$; Figure 4c) for all the samples first exhibit increment with rising temperature in the low-temperature range before reaching plateau. The maximum power factors of the 0.005, 0.01, and 0.015 Pb samples are 1.15, 1.00, and 0.86 mW m^{-1} K^{-2}, respectively.

The thermal conductivity can be expressed by $\kappa = C_p \times D_T \times \rho$, where C_p (J g^{-1} K^{-1}) is the specific heat obtained by differential scanning calorimetry (Figure S14c, Supporting Information), D_T (m^2 s^{-1}) is the thermal diffusivity measured by the laser flash method (Figure S14d, Supporting Information), and ρ is the density (≈ 5.30 g cm^{-3}, relative density = 78%, determined geometrically). The dependence of total thermal conductivity (κ_{tot}) on temperature is presented in Figure 4d. The κ_{tot} of the 0.005 Pb sample decreases from 0.60 W m^{-1} K^{-1} at 313 K to 0.57 W m^{-1} K^{-1} at 388 K and then increases to 0.64 W m^{-1} K^{-1} at 538 K. Similarly, the κ_{tot} of the 0.010 Pb and 0.015 Pb samples show an initial decrease and subsequent increase as the temperature goes high.

Finally, the temperature dependence of figure of merit is plotted in Figure 4e. Clearly the zT of the 0.005 Pb sample is better than those of the other two compositions below 450 K, reaching a peak of 0.84 at 438 K, but starts to drop at >450 K. The zT of the 0.010 Pb sample increases from 0.35 (at 313 K) to 1.02 (at 513 K) and maintains higher than 1.0 (at 613 K) before dropping below 1.0 (0.95 at 638 K). The zT of the 0.015 Pb sample increases steadily from 0.21 (at 313 K) to 0.95 (638 K). Moreover, the high performance is maintained the same after repeated tests (Figure S16, Supporting Information). The thermoelectric properties of the 0.020 and 0.040 Pb samples are also shown in Figure S15f,g (Supporting Information).

To investigate the origin of the high zT values in the low-medium temperature (513–613 K) range, we have conducted a series of experimental analysis and theoretical modeling. First, diffuse reflectance Fourier transform infrared spectroscopy is used to determine the optical bandgap for several Pb concentrations at room temperature (**Figure 5**d and Figure S17, Supporting Information). By definition of the Burstein–Moss effect, $E_g = E_{g,0} + \Delta E_g^{BM}$ (dashed line in Figure 5d), increased degeneracy pushes the Fermi level deeper into the band (valance band for our p-type material), causing the effective bandgap, E_g, to widen as minority carriers must not only cross the intrinsic bandgap, E_{g0}, but also reach the lowest unoccupied level in the band. The extra energy required for these carriers to cross the gap is called the Burstein–Moss shift, defined in the context of parabolic bands as $\Delta E_g^{BM} = (\hbar^2/2 m_{vc}^*)(3\pi^2 n)^{2/3}$ where m_{vc}^* is the reduced effective mass of the valance and conduction band (a value of unity was used in Figure 5d), and n is carrier concentration. While there may be a renormalization term added to account for carrier screening effects,[28] the trend in the observed optical gap with Pb concentration (Figure 5d) clearly follows a Burstein–Moss-type behavior, as also seen in Pb-doped Bi$_2$Te$_3$ (values shown as green squares in Figure 5d were calculated from data taken from ref. [29]). The increase in effective bandgap is further corroborated by the observed increase in the Goldsmid–Sharp gap[30] (Table S1 and blue markers in Figure S17b, Supporting Information) calculated empirically from the Seebeck data.
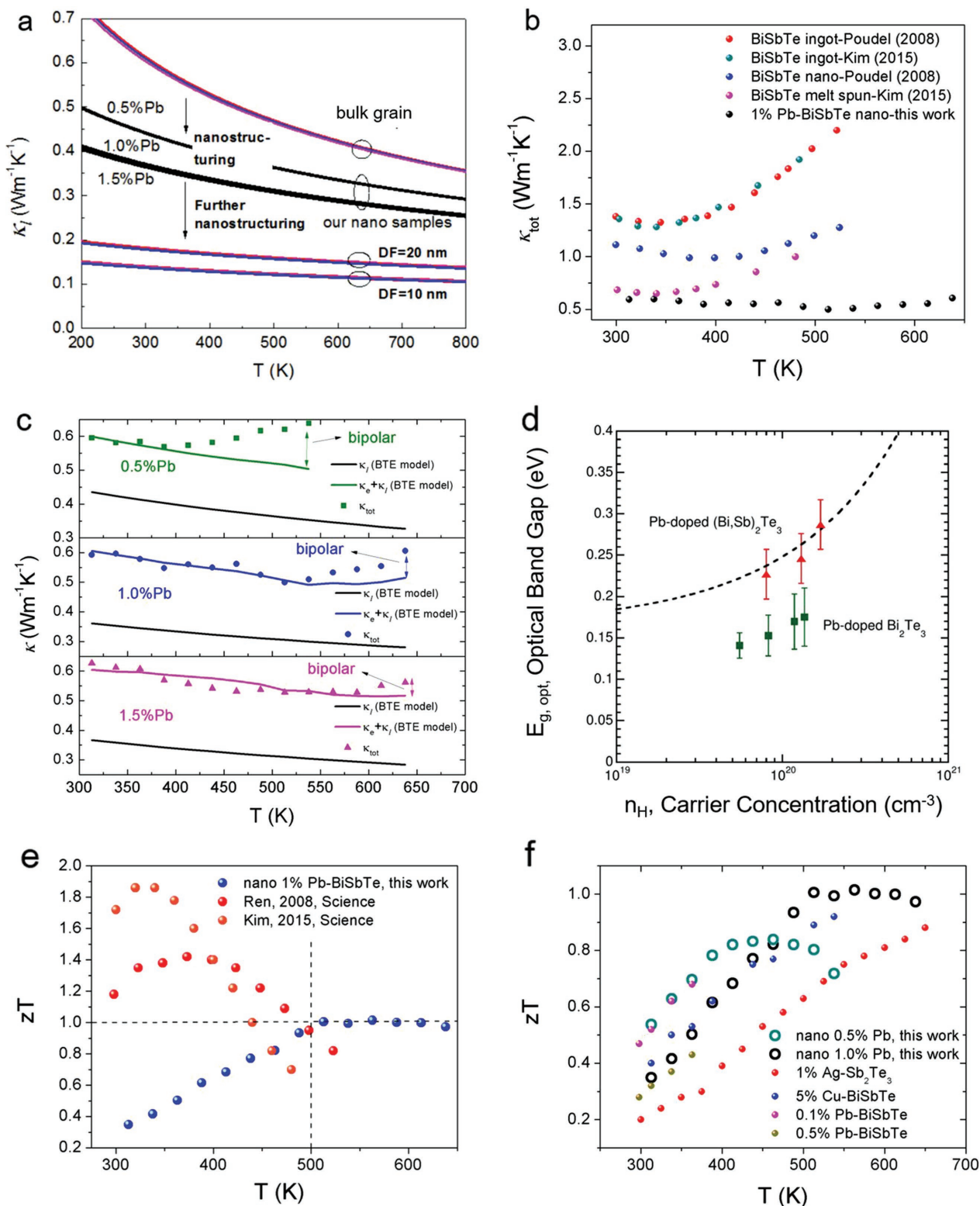
Generally, theoretical modeling of the electrical conductivity and Seebeck coefficient of different Pb-BiSbTe samples is done using the Boltzmann transport equation (BTE).[31] We considered both conduction and valence bands in the modeling to quantify the bipolar transport effect on these material properties. The band structure parameters used in the BTE simulation were obtained by fitting the electronic density of states (DOS)

of Bi$_2$Te$_3$ from the first-principle band structure calculations.[32] We used the modified Kane model in the DOS fitting to account for the nonparabolicity in the bands, and included two conduction bands and two valence bands to fit the DOS over a wide energy range.[31] More information can be found in the Supporting Information. The same band parameters that were used for Bi$_2$Te$_3$ were used for our materials except for the bandgap, which was adjusted to best fit the experimental electrical conductivities and Seebeck coefficients of our samples. As a result, a bandgap of 0.22 eV was used in our simulations, and this value is consistent with the Goldsmid–Sharp energy gap (Table S1, Supporting Information). Note that this bandgap value used in our BTE simulation does not include the Burstein–Moss shift shown in the optical bandgap. **Table 1** summarizes the band structure and material parameters used in the BTE simulation. As shown in Table 1, the hole mobility is reduced with increased Pb, which is due to the increased carrier scattering with defects and interfaces.

The calculated electron transport properties are shown as solid curves in Figure 4a,b, and match well with the experimental results (markers in Figure 4a,b). With increased Pb doping and corresponding higher carrier concentration, the Pb-BiSbTe samples show an increased Fermi level away from the valence band maximum, according to BTE calculations (Figure S14e, Supporting Information), in agreement with the Burstein–Moss shift discussed above. Increased majority carrier (hole) concentration, occupying higher energy levels, results in reduced thermal excitation of minority carriers (electrons), thus the net Seebeck coefficient remained high with delayed bipolar effects. As a result, both the peak in Seebeck coefficient and plateau in power factor ($S^2\sigma$) were shifted to a higher temperature with increased Pb doping, extending the plateau of zT to higher temperatures. As one can see in Figure 4f, our 1% Pb (8.00×10^{19} cm^{-3}) and 1.5% Pb (1.25×10^{20} cm^{-3}) samples are well optimized in terms of carrier concentration to achieve a maximum power factor at 500 and 600 K, respectively.

Besides the tuned power factor, the total thermal conductivity of the nanocomposite is pronouncedly reduced compared to bulk grain materials reported in the literature, and comparable to the κ_{tot} of other nanostructured BiSbTe at room temperature (Figure 5b). Moreover, due to the delayed onset of bipolar conduction in our Pb-doped material, the thermal conductivity remains consistently low over the investigated temperature range, whereas the other studies report a notable increase in κ_{tot} above 400 K (Figure 5b).[8,10] We can model the various contributions to thermal conductivity, as κ_{tot} is expressed as $\kappa_e + \kappa_l + \kappa_{bi}$, in which κ_e is electronic contribution, κ_l is the lattice part, and κ_{bi} is the bipolar thermal conductivity. κ_e is estimated as $L\sigma T$, where L is the Lorenz number (calculated through BTE; Figure S14f, Supporting Information) and σ is the electrical conductivity. We find that the electronic contribution to the κ_{tot} is around 25–40% depending on the doping level (Table S2, Supporting Information).

From the TEM (Figure 3e and the nanograin as indicated by yellow boundaries in Figure S11, Supporting Information) and SEM (Figure S12, Supporting Information) study of PbTe-Bi$_{0.7}$Sb$_{1.3}$Te$_3$, both the nanograins of PbTe and Bi$_{0.7}$Sb$_{1.3}$Te$_3$ do not grow much in size upon SPS. XRD is also used to estimate the grain size, d, based on the Scherrer equation ($d = K\lambda/\beta\cos\theta$,

ADVANCED
SCIENCE NEWS
www.advancedsciencenews.com

ADVANCED
MATERIALS
www.advmat.de

COMMUNICATION

Figure 5. Experimental and theoretical study on the origin of high zT. a) Simulated $\kappa_{lattice}$ as a function of grain diameter (effect of nanostructuring); b) a comparison of κ_{total} of our nano-1.0% Pb-BiSbTe samples with literature values of BiSbTe-based materials;[8,10] c) a breakdown of thermal conductivity: K_i, $K_i + K_e$ and K_{tot}; d) the optical bandgap of select Pb-BiSbTe samples with different carrier concentrations (red triangles), as compared to single parabolic band (SPB)-derived bandgaps (dash line) and the bandgaps of Pb-doped Bi_2Te_3 (green squares);[29] e) the zT of our 1% Pb-doped nanocomposite in comparison with previously reported undoped BiSbTe;[8,10] and f) the zT of our nanocomposites in comparison with doped BiSbTe in the literature (1% Ag-Sb_2Te_3,[16] 5% Cu-$Bi_{0.5}Sb_{1.5}Te_3$,[18] 0.1% and 0.5% Pb-$Bi_{0.4}Sb_{1.6}Te_3$[15]).

Table 1. Band structure and material parameters used in BTE simulations for the electron transport modeling of the Pb-doped $Bi_{0.7}Sb_{1.3}Te_3$ samples at room temperature.

Parameter	0.5% Pb	1.0% Pb	1.5% Pb
Electronic bandgap [eV]		0.22	
Electron effective mass [m_0]		0.63	
Hole effective mass [m_0]		1.19	
Hole concentration [cm^{-3}]	4×10^{19}	8×10^{19}	1.1×10^{20}
Hole mobility [$cm^2 V^{-1} s^{-1}$]	58.6	39.2	32.0

where K is the shape factor (0.9), λ is the X-ray wavelength, β is the full width at half maximum (FWHM, averaged on several peaks), and θ is the Bragg angle, $d = 61$, 38, and 50 nm for 0.005, 0.010, and 0.015 Pb samples, respectively.[33] The nanosize of the grain is likely to be benefited from the fast (5 min) and efficient sintering process of SPS, as compared to conventional technique such as melt ingot forming and hot pressing. Consequently, κ_l can be strongly reduced in contrast to the bulk-grain counterpart, due to the intensified grain boundary scattering of phonons in our nanocomposites.

This is corroborated by the theoretical modeling of κ_l. Since Bi_2Te_3 and Sb_2Te_3 have three dispersive acoustic branches and many low-energy optical branches, we use a phonon BTE model[34] together with an exact full phonon dispersion obtained from first-principles (density functional theory) calculations[35] rather than a simple Debye model (only one branch with linear dispersion). The total phonon scattering rate for the phonon mode ($\mathbf{k},\nu$) is given by Matthiessen's rule:

$$\frac{1}{\tau_{ph}(\mathbf{k},\nu)} = \frac{1}{\tau_p(\mathbf{k},\nu)} + \frac{1}{\tau_{mass}(\mathbf{k},\nu)} + \frac{1}{\tau_{pb}(\mathbf{k},\nu)} + \frac{1}{\tau_d(\mathbf{k},\nu)} + \frac{1}{\tau_b(\mathbf{k},\nu)} \tag{1}$$

where $\mathbf{k}$ and ν specify the phonon wave vector and dispersion branch, respectively. The terms on the right-hand side are the scattering rates induced by the lattice anharmonicity (p, determined by the pristine Bi_2Te_3 and Sb_2Te_3), Bi-Sb alloy mass disorder (mass, determined by Bi-Sb atomic ratio), Pb impurity (Pb, determined by Pb concentration), other defects (d, including antisites, vacancies, dislocations, distortion, etc., g_{other} as a fitting parameter), and grain boundaries (b, grain diameter DF as a fitting parameter), respectively. Based on the phonon BTE, the lattice thermal conductivity can be calculated by (see the Supporting Information for more details):

$$K_l = \frac{4\pi}{3} \frac{1}{(2\pi)^3} \sum_\nu \left[\frac{2}{3} \int_x + \frac{1}{3} \int_z \right] \frac{\hbar^2 \omega^2(\mathbf{k},\nu)}{k_B T^2} \times \frac{e^{\frac{\hbar\omega(\mathbf{k},\nu)}{k_B T}}}{\left(e^{\frac{\hbar\omega(\mathbf{k},\nu)}{k_B T}} - 1 \right)^2} v^2(\mathbf{k},\nu)\tau(\mathbf{k},\nu)k^2 dk \tag{2}$$

The only two fitting parameters g_{other} and DF are fitted to best reproduce the low-temperature experimental lattice thermal conductivity when the bipolar effect is negligible. We find that

the κ_l of Pb-BiSbTe is mainly determined by the scattering induced by the alloy mass disorder, grain boundaries, and other defects, whereas it is less influenced by the Pb impurity since the Pb concentration is relatively small (Figure S19, Supporting Information). At 300 K, the alloy mass disorder reduces the κ_l of the imaginary mixture of PbTe, Bi_2Te_3, and Sb_2Te_3 from 2.1 W m^{-1} K^{-1} to 0.74 W m^{-1} K^{-1}. The low κ_l achieved in our materials are mainly benefited from the large amounts of defects and small grain sizes. The antisites, vacancies, dislocations, distortion, etc., further reduce κ_l to 0.61 W m^{-1} K^{-1}. The nanograin in 0.005, 0.010, and 0.015 Pb sample reduces it further to 0.442, 0.365, and 0.371 W m^{-1} K^{-1}, respectively (Figure 5a). The lowest value of κ_l (0.365 W m^{-1} K^{-1} at 313 K) reported here is comparable with the lowest reported κ_l (0.31–0.33 W m^{-1} K^{-1} at 300 K) in BiSbTe nanocomposites from the literature, and much lower than that of bulk BiSbTe.[10,20] As indicated in Figure 5a, if the grain size is further reduced to 10–20 nm, κ_l can be reduced to 0.15–0.20 W m^{-1} K^{-1}, which is similar to that of Bi_2Te_3/Sb_2Te_3 superlattices.[36]

The calculated temperature-dependent lattice thermal conductivities are compared to the experimental values in Figure 5c. They match well at low temperatures while they start to deviate from each other at 370, 530, and 570 K for the 0.5%, 1%, and 1.5% Pb-doped BiSbTe nanocomposites, respectively. This indicates that the κ_{bi}, the difference between κ_{tot} and $\kappa_l + \kappa_e$, is suppressed more as the Pb doping concentration increases (Figure 5c). This is in agreement with the temperature-dependent Seebeck data (Figure 4b), and is also the result of the Burstein–Moss shift discussed above, where the optical bandgap increases with increasing carrier concentration (Figure 5d).[37] As a result, the onset temperature of increasing thermal conductivity due to the bipolar effect has been significantly shifted to higher temperatures compared to that of the undoped BiSbTe in the literature (Figure 5b).[8,20]

For our nanocomposite with 1% Pb, the zT reaches 1.0 at 513 K and maintains unity until 613 K, thanks to the optimized $S^2\sigma$ and suppressed κ_l and κ_{bi}. For all previously reported bulk and nanoundoped BiSbTe, the zT drops below 1 for temperatures above 500 K (Figure 5e) due to bipolar contributions to the thermal conductivity (Figure 5b) and Seebeck coefficient (not shown).[8,13,20] For doped-BiSbTe, $zT = 1$ has also never been achieved in this temperature range (Figure 5f), due to the impaired carrier mobility μ from doping and unreduced κ_l.[15–19] Compared with state-of-the-art undoped BiSbTe, the zT peak of our Pb-BiSbTe nanocomposite is notably shifted to higher temperature, by more than 100 K (Figure 5e). More significantly, in contrast to previously doped BiSbTe materials, the unity plateau of zT lasts from 500 to 600 K, giving a high average value of zT (Figure 5f).

For the low-medium temperature range (500–600 K), which is quite crucial for the recovery of low-grade waste heat, material candidates with $zT > 1$ are extremely limited. GeTe[38] and MgAgSb[39] were found to have decent zT. However, Ge and Ag are precious and rare elements. CdSb[40] and NaPbSbTe[22] are also strong candidates, but use large amounts of toxic elements (Cd, Pb). Doped SnSe single crystals have the best zT along the b-axis,[41] but it is highly anisotropic and fragile, having much lower performance along other crystallographic directions. Our Pb-BiSbTe nanocomposite is based on nanocrystalline

BiSbTe, which is cost-efficient, less toxic (using only 1% Pb), and mechanically rigid. Thus, it can be readily integrated into commercial modules as a p-type leg and can replace the mid-temperature PbTe alloy materials in the 500–600 K range.

In conclusion, we have fabricated tunable PbTe-BiSbTe nanoheterostructures using a scalable, repeatable, wet chemical synthesis method that can be used beyond the field of thermoelectrics. Nanocomposites ($\approx$40 nm grain size) can be made from the nanoheterostructures by spark plasma sintering. The thermoelectric properties were enhanced by tuning the power factor and delaying bipolar conduction through controlled Pb-doping, as well as reducing the lattice thermal conductivity through nanostructuring. These p-type materials have a $zT > 1$ in the low-medium temperature range (513–613 K), making them better than previously reported BiSbTe materials for low grade waste heat recovery.

Supporting Information

Supporting Information is available from the Wiley Online Library or from the author.

Acknowledgements

[1] a) G. J. Snyder, E. S. Toberer, *Nat. Mater.* **2008**, *7*, 105; b) W. Liu, X. Yan, G. Chen, Z. Ren, *Nano Energy* **2012**, *1*, 42; c) L.-D. Zhao, V. P. Dravid, M. G. Kanatzidis, *Energy Environ. Sci.* **2014**, *7*, 251.

[2] J. P. Heremans, V. Jovovic, E. S. Toberer, A. Saramat, K. Kurosaki, A. Charoenphakdee, S. Yamanaka, G. J. Snyder, *Science* **2008**, *321*, 554.

[3] Y. Pei, X. Shi, A. LaLonde, H. Wang, L. Chen, G. J. Snyder, *Nature* **2011**, *473*, 66.

[4] Y. Zhang, J.-H. Bahk, J. Lee, C. S. Birkel, M. L. Snedaker, D. Liu, H. Zeng, M. Moskovits, A. Shakouri, G. D. Stucky, *Adv. Mater.* **2014**, *26*, 2755.

[5] L. D. Hicks, M. S. Dresselhaus, *Phys. Rev. B* **1993**, *47*, 16631.

[6] a) J.-S. Rhyee, K. H. Lee, S. M. Lee, E. Cho, S. I. Kim, E. Lee, Y. S. Kwon, J. H. Shim, G. Kotliar, *Nature* **2009**, *459*, 965; b) H. Liu, X. Shi, F. Xu, L. Zhang, W. Zhang, L. Chen, Q. Li, C. Uher, T. Day, G. J. Snyder, *Nat. Mater.* **2012**, *11*, 422.

[7] K. F. Hsu, S. Loo, F. Guo, W. Chen, J. S. Dyck, C. Uher, T. Hogan, E. K. Polychroniadis, M. G. Kanatzidis, *Science* **2004**, *303*, 818.

[8] B. Poudel, Q. Hao, Y. Ma, Y. Lan, A. Minnich, B. Yu, X. Yan, D. Wang, A. Muto, D. Vashaee, X. Chen, J. Liu, M. S. Dresselhaus, G. Chen, Z. Ren, *Science* **2008**, *320*, 634.

[9] K. Biswas, J. He, I. D. Blum, C.-I. Wu, T. P. Hogan, D. N. Seidman, V. P. Dravid, M. G. Kanatzidis, *Nature* **2012**, *489*, 414.

[10] S. I. Kim, K. H. Lee, H. A. Mun, H. S. Kim, S. W. Hwang, J. W. Roh, D. J. Yang, W. H. Shin, X. S. Li, Y. H. Lee, G. J. Snyder, S. W. Kim, *Science* **2015**, *348*, 109.

[11] H. J. Goldsmid, R. W. Douglas, *Br. J. Appl. Phys.* **1954**, *5*, 386.

[12] T. Zhu, L. Hu, X. Zhao, J. He, *Adv. Sci.* **2016**, *3*, 1600004.

[13] H. Goldsmid, *Mater.* **2014**, *7*, 2577.

[14] A. D. LaLonde, Y. Pei, H. Wang, G. Jeffrey Snyder, *Mater. Today* **2011**, *14*, 526.

[15] S. Ganguly, C. Zhou, D. Morelli, J. Sakamoto, C. Uher, S. L. Brock, *J. Solid State Chem.* **2011**, *184*, 3195.

[16] L. P. Hu, T. J. Zhu, X. Q. Yue, X. H. Liu, Y. G. Wang, Z. J. Xu, X. B. Zhao, *Acta Mater.* **2015**, *85*, 270.

[17] W.-T. Chiu, C.-L. Chen, Y.-Y. Chen, *Sci. Rep.* **2016**, *6*, 23143.

[18] J. Cui, W. Xiu, H. Xue, *J. Appl. Phys.* **2007**, *101*, 123713.

[19] Y. Xiao, J.-y. Yang, Q.-h. Jiang, L.-w. Fu, Y.-b. Luo, M. Liu, D. Zhang, M.-y. Zhang, W.-x. Li, J.-y. Peng, F.-q. Chen, *J. Mater. A* **2014**, *2*, 20288.

[20] L.-P. Hu, T.-J. Zhu, Y.-G. Wang, H.-H. Xie, Z.-J. Xu, X.-B. Zhao, *NPG Asia Mater.* **2014**, *6*, e88.

[21] S. Wang, J. Yang, T. Toll, J. Yang, W. Zhang, X. Tang, *Sci. Rep.* **2015**, *5*, 10136.

[22] P. F. P. Poudeu, J. D'Angelo, A. D. Downey, J. L. Short, T. P. Hogan, M. G. Kanatzidis, *Angew. Chem.* **2006**, *118*, 3919.

[23] a) S. W. Finefrock, H. Yang, H. Fang, Y. Wu, *Annu. Rev. Chem. Biomol. Eng.* **2015**, *6*, 247; b) R. J. Mehta, Y. Zhang, C. Karthik, B. Singh, R. W. Siegel, T. Borca-Tasciuc, G. Ramanath, *Nat. Mater.* **2012**, *11*, 233; c) A. Soni, Y. Shen, M. Yin, Y. Zhao, L. Yu, X. Hu, Z. Dong, K. A. Khor, M. S. Dresselhaus, Q. Xiong, *Nano Lett.* **2012**, *12*, 4305.

[24] H. Fang, T. Feng, H. Yang, X. Ruan, Y. Wu, *Nano Lett.* **2013**, *13*, 2058.

[25] H. Yang, J.-H. Bahk, T. Day, A. M. S. Mohammed, G. J. Snyder, A. Shakouri, Y. Wu, *Nano Lett.* **2015**, *15*, 1349.

[26] L. Carbone, P. D. Cozzoli, *Nano Today* **2010**, *5*, 449.

[27] Y. Pei, A. F. May, G. J. Snyder, *Adv. Energy Mater.* **2011**, *1*, 291.

[28] A. Walsh, J. L. F. Da Silva, S.-H. Wei, *Phys. Rev. B* **2008**, *78*, 075211.

[29] a) T. Plecháček, P. Lošť'ák, J. Navrátil, T. Černohorský, *Cryst. Res. Technol.* **1998**, *33*, 911; b) T. Plecháček, J. Navrátil, J. Horák, P. Lošť'ák, *Philos. Mag.* **2004**, *84*, 2217.

[30] Z. M. Gibbs, H.-S. Kim, H. Wang, G. J. Snyder, *Appl. Phys. Lett.* **2015**, *106*, 022112.

[31] J.-H. Bahk, A. Shakouri, *Phys. Rev. B* **2016**, *93*, 165209.

[32] C. Jeong, R. Kim, M. Luisier, S. Datta, M. Lundstrom, *J. Appl. Phys.* **2010**, *107*, 023707.

[33] B. E. Warren, *X-Ray Diffraction*, Addison-Wesley Publishing Co, Reading, MA, USA **1969**.

[34] T. Feng, X. Ruan, *J. Nanomater.* **2014**, *2014*, 206370.

[35] V. Chis, I. Y. Sklyadneva, K. A. Kokh, V. A. Volodin, O. E. Tereshchenko, E. V. Chulkov, *Phys. Rev. B* **2012**, *86*, 174304.

[36] R. Venkatasubramanian, E. Siivola, T. Colpitts, B. O'Quinn, *Nature* **2001**, *413*, 597.

[37] M. G. Zachary, L. Aaron, G. J. Snyder, *New J. Phys.* **2013**, *15*, 075020.

[38] E. Hazan, O. Ben-Yehuda, N. Madar, Y. Gelbstein, *Adv. Energy Mater.* **2015**, *5*, 1500272.

[39] H. Zhao, J. Sui, Z. Tang, Y. Lan, Q. Jie, D. Kraemer, K. McEnaney, A. Guloy, G. Chen, Z. Ren, *Nano Energy* **2014**, *7*, 97.

[40] S. Wang, J. Yang, L. Wu, P. Wei, J. Yang, W. Zhang, Y. Grin, *Chem. Mater.* **2015**, *27*, 1071.

[41] L.-D. Zhao, G. Tan, S. Hao, J. He, Y. Pei, H. Chi, H. Wang, S. Gong, H. Xu, V. P. Dravid, C. Uher, G. J. Snyder, C. Wolverton, M. G. Kanatzidis, *Science* **2016**, *351*, 141.